

GEOMETRICAL IMPERFECTION AND ADIABATIC SHEAR BANDING

D. Rittel¹, Z. G. Wang and A. Dorogoy
Faculty of Mechanical Engineering
Technion
32000 Haifa, Israel

¹ *Corresponding author: merittel@technion.ac.il*

ABSTRACT

This work addresses the effect of small geometrical imperfections on adiabatic shear band (ASB) formation. The separate effect of the length and radius of short notches is systematically investigated in AM50 and Ti6Al4V alloys, using shear compression specimens. It is observed that the length of the imperfection does not influence ASB formation in these experiments. By contrast, the notch-root radius appears to be the dominant parameter for the two materials, in perfect agreement with the analytical predictions of Dinzart et al. (1994). The distribution of deformation energy over the gauge length is modeled numerically. The calculated average dynamic deformation energy levels are quite similar to those that are measured for the two investigated alloys. It is concluded that the global measure of the dynamic deformation energy provides valuable information about ASB failure from geometrical imperfections.

Keywords: geometrical imperfection, adiabatic shear band, dynamic deformation energy, notch geometry.

GEOMETRICAL IMPERFECTION AND ADIABATIC SHEAR BANDING

INTRODUCTION

Adiabatic shear banding (subsequently referred to as ASB) is a catastrophic failure mechanism that may develop in certain ductile materials which are subjected to dynamic loading (Tresca, 1979). The phenomenon itself consists of a narrow band (for a discussion on the width of the band, see e.g. Merzer, 1982) of sheared material, in which the local temperature may reach a significant fraction of the melting temperature, as a result of thermomechanical coupling effects. A large body of literature can be found on the metallurgical aspects of ASB, that emphasize mostly microstructural aspects, including phase transformation and dynamic recrystallization (these subjects are covered in detail in Bai and Dodd (1992), and in Meyers (1994)). ASB is treated as an instability, either material or structural. The classical explanation of Zener and Hollomon (1944) outlines the conflicting influences of strain hardening and thermal softening, to reach a point where the material no longer hardens, loses its load bearing capability and fails in a localized mode. In this case, the main destabilizing factor is identified as the thermal softening effect, which can be introduced in various constitutive models to identify a critical strain to failure (for a review, see e.g. Bai and Dodd (1992)). Alternatively, one may consider a small geometrical imperfection, whose growth and stability can be investigated. Loss of stability in a localized mode is identified as ASB formation. These issues are investigated analytically (Wright, 2002) or numerically with suitable failure criteria, the most popular to date being that of a critical strain to failure (e.g. Batra, 1990a, b; Batra and Gummalla, 2000).

Among the very few experimental works dedicated to ASB formation in the mechanical sense, seminal contributions were made by Duffy and coworkers (Marchand and Duffy (1988), Duffy and Chi (1992), Liao and Duffy (1998)), who systematically investigated the phenomenon using high rate torsion of thin-walled specimens, into which a small geometrical imperfection had been deliberately introduced. These authors pioneered temperature measurements in the shear band using non-contact infrared radiometry. A clear picture appears from these works, in which the temperature rises noticeably, at the final stages of the deformation process

only, presumably once the shear band has formed. Prior to this stage, the temperature rise is very modest, as also observed by Clos and Schreppel (2003).

The experiments of Duffy and coworkers were all carried out on torsion specimens that contained small circumferential notches (local reduction in wall thickness), whose role is to assist in locating and localizing the shear deformation (Molinari and Clifton, 1987). Yet, the role of the geometrical imperfection (defect) in itself was not the main concern of these works, and in fact, the reported results point to conflicting evidence, depending of the material, as to the influence of the length of the defect on ASB formation (Duffy and Chi (1992)). One should note that these works are closely connected to the analysis of Molinari and Clifton (1987), in which the geometry of the defect is defined as a trigonometric function so that the length and root radius of the defect are intrinsically related. Here, one should mention the work of Dinzart et al. (1994) who investigated the effect of the sharpness and the length of the geometric defect on ASB failure. Their conclusion was that the sharpness of the defect is the governing factor. However, it appears from the literature that there is no systematic experimental evidence on the relation between geometrical defect and ASB formation, in which the length and the root radius of the defect are considered separately. This is the main issue addressed in this paper.

Rittel et al. (2006) investigated ASB formation in macroscopically smooth specimens (homogeneous nucleation) and suggested that the dynamically stored energy of cold work (Bever et al., 1973) could be considered as an alternative or complementary criterion to the classical thermal softening model, as discussed by Nowacki and Zarka (1979) Energy considerations tie naturally mechanical and microstructural aspects, since the stored energy of cold work is characteristic of the microstructural evolution during the deformation process. This concept will be used in the present work.

Therefore, the aim of the present work is to present a systematic investigation of the influence of geometrical imperfections (length and root radius) on ASB formation, within the above mentioned framework of dynamic deformation energy (Rittel et al., 2006).

We first introduce the experimental setup, materials and specimens used in this study. This section is followed by a two-part description of the experimental results. The first part is introductory and it extends the concept of dynamic deformation energy by presenting new results for annealed Ti6Al4V alloy, just as was done for AM50 magnesium alloy (Rittel et al., 2006). The main purpose of this section is to show that

the dynamic response of Ti6Al4V can be addressed using the exact same framework as AM50. The second, and main part of this work, addresses the influence of small imperfections. It is shown that while the length of the defect cannot be correlated with the mechanical energy or failure strain at for ASB formation, a clear trend can be identified concerning the root-radius (sharpness) of the imperfection. Detailed numerical modeling of the dynamically sheared imperfection is presented next, followed by a discussion section and concluding remarks.

EXPERIMENTAL

Materials and specimens

Two materials were investigated in this study. The first is a magnesium-aluminum alloy AM50 (ASTM B94), supplied as cylindrical rods (Rittel et al., 2006). Microstructural characterization, using transmission electron microscopy (TEM) and Energy Dispersive X-ray Analysis (EDX), reveals an Al-Mg solid solution (matrix) which contains elongated (typically 1 μm long) β phase ($\text{Mg}_{17}\text{Al}_{12}$) and Al_8Mn_5 precipitates. The second material is a commercial titanium alloy (Ti6Al4V), supplied in the annealed condition.

Two specimen geometries were used throughout this study, for both quasi-static and dynamic compression tests. Compression cylinders were machined from the rods, with a typical diameter of 9 mm and height of 4 mm. The second specimen used in this study is the shear compression specimen (SCS, Rittel et al., 2002). This specimen consists of a pair of diametrically opposed grooves that make a 45° angle with the longitudinal axis of a cylinder (Figure 1). The SCS has been thoroughly validated numerically (Dorogoy and Rittel, 2005a, b), and used in several experimental studies as well (Rittel et al., 2002).

One of its main advantages is that it can be used indifferently for quasi-static and dynamic (high-rate) tests, with the same data reduction technique. The latter consists of mapping the measured loads and displacements into equivalent stress (σ_e) and strain (ϵ_e) in the gauge section comprised between the grooves. This process requires preliminary numerical simulations, but the final validation comes from a comparison of the stress-strain characteristics of the investigated material, using both SCS and cylindrical specimens. In that case, one has to make sure that the flow curves match

each other so that specimen independence can be established. The basic equations for the equivalent stress and strain in the gauge section are given by:

$$\varepsilon_e = \varepsilon_y + K_3 \frac{(d - d_y)}{h} + K_4 \left(\frac{d - d_y}{h} \right)^2 + K_5 \left(\frac{d - d_y}{h} \right)^3 \quad (1)$$

$$\sigma_e = K_1 (1 - K_2 \varepsilon_e) \frac{P}{Dt} \quad (2)$$

where d is the prescribed vertical displacement of the gage section, and P is the applied load. The terms ε_y and d_y correspond to the strain and displacement values at the yield point. As mentioned before, the K coefficients must be determined numerically, and the degree of the polynomial fitting is determined by accuracy considerations, noting that in most cases, 3 coefficients are sufficient to accurately describe the material behavior, while higher order approximation may be necessary in other cases, such as AM50.

Small notches, of carefully controlled root-radius and length were machined by electro-erosion, as shown in Figure 2. A systematic array of lengths and root-radii was devised, as summarized in Table 1 for AM50 and Ti6Al4V alloys.

A preliminary numerical study (the numerical model is described in detail in the sequel) of each material was carried out to determine the various K coefficients, whose values are given in Table 2, for the specimen shown in Figure 1. The introduction of short notches of varying root radius is expected to affect the average stress and strain distribution in the gauge section. This point was therefore checked by means of numerical simulations. The results, listed in Table 2, show that the K coefficients of AM50 are insensitive to the presence of the small notches. The coefficients of Ti6Al4V, on the other hand, are slightly dependent on the notch root radius.

Mechanical testing systems

Quasi-static testing was performed on a servo-hydraulic testing machine (MTS-810), under displacement control. Dynamic tests were performed using a split Hopkinson pressure bar (Kolsky, 1949), made of 17-4 PH steel bars with a diameter of 19.05 mm. For the sake of brevity, the data reduction technique will not be described here,

as it is quite standard. However, it will only be mentioned that specimen equilibrium was ascertained in each test, by comparing the applied forces on each side of the specimen.

RESULTS

Dynamic shear band toughness – Ti6Al4V

Static-dynamic tests

In a recent paper, Rittel et al. (2006) suggested that the dynamic deformation energy can be considered as a criterion (toughness) for ASB formation. Various results were shown for the AM50 alloy, and in this section, we will present new results for the annealed Ti6Al4V alloy. The first series of tests consisted of quasi-static loading of SCS specimens, followed by impact loading of the same specimens. Typical composite stress-strain curves are shown in Figure 3, and it can be noted that the total strain to failure (indicated by an arrow) increases sensibly with the quasi-static level of pre-strain. Figure 3 shows that a critical strain criterion does not take into account the thermomechanical history of the material, and in that respect, Ti6Al4V is identical to AM50.

The dynamic deformation energy (integral of the dynamic stress-strain curve until the onset of failure where the stress starts to drop) can be calculated and plotted as a function of the quasi-static pre-strain level ϵ_{FS} (determined from separate quasi-static tests), as shown in Figure 4.

This figure shows that the mechanical energy remains relatively constant for a large range of quasi-static pre-strain levels of up to about 45% of the monotonic static strain to failure ($\epsilon_{FS}^{Ti6Al4V} = 0.34$), with a typical value of $W_D^{Ti6Al4V} = 3.48 \times 10^8 \text{ J/m}^3$, to be used subsequently. A similar observation was also reported for AM50 (Rittel et al., 2006). It can also be noted that Ti6Al4V exhibits a modest strain hardening at high strain-rates. Consequently, in this specific case, a critical strain criterion is a particular case of the energy criterion since the stress level is almost constant.

Dynamic-dynamic tests

The dynamic-dynamic test is an interrupted dynamic test in which the specimen is dynamically loaded to a defined strain level, allowed to cool for some 15 min, followed by dynamic reloading to failure. Typical results are shown in Figure 5,

which show that, contrary to the static-dynamic tests, the interrupted tests are identical to single-shot tests, within minor variations from test to test. For this material, a typical value for the dynamic failure strain is $\epsilon_{FD}^{Ti6Al4V} = 0.25$.

High temperature dynamic tests

The homogeneous temperature rise that is expected to develop in the gauge section of the specimen, prior to the localization phase, can be estimated by converting the mechanical energy into thermal energy. This simple exercise shows that, assuming that the entire mechanical energy goes into heat, the homogeneous temperature rise $\Delta T_{hom} = 147\text{ K}$, so that $T_{hom-max} = 445\text{ K}$. To gain additional insight into the effects of a temperature rise on ASB formation, dynamic tests were performed over a range of temperatures ($RT = 297\text{ K}$ to $T = 573\text{ K}$), with the specimen being impacted inside a specially adapted furnace. Figure 6 shows the recorded stress-strain curves (A), and (B) the dynamic deformation energy as a function of the normalized test temperature (w/r to the melting temperature, $T_m = 1873\text{ K}$). These figures show that, even at test temperatures in excess of $T_{hom-max}$, the dynamic deformation energy remains almost unaffected, however the material loses almost all of its strain hardening capacity upon heating. The insensitivity of the dynamic deformation energy to the test temperature indicates again that thermal softening effects may not be the only cause for ASB formation.

Table 3 summarizes the various mechanical parameters that were obtained for AM50 (Rittel et al., 2006) and Ti6Al4V alloys. These parameters are used in the next section to normalize the results related to notched specimens. To conclude this section, it can be noted that the experiments reported here on Ti6Al4V are of identical nature to those previously conducted on AM50 alloy, illustrating the concept of a dynamic deformation energy for ASB formation.

Dynamic tests of notched specimens

Notched SCS: influence of the notch length

The dynamic strain to failure (indicated by arrows in Figure 3) is plotted as a function of the length of the notch (Figure 2) in Figure 7 for AM50 (A) and of Ti6Al4V (B), respectively. The failure strain has been normalized with respect to that of un-notched

specimens (ϵ_{FD} , Table 3), to allow for comparison between AM50 and Ti6Al4V alloys.

It should be noted that, for each alloy, some specimens with notch root-radii of $\rho=0.15\text{mm}$ and $\rho=0.30\text{mm}$ did not fail from the notch-tip itself. Rather, fracture proceeded along the gauge fillet, as if there were no notch in the gauge section. All in all, Figure 7 shows that the introduction of a notch causes some decrease in the failure strain, but the latter is not clearly related to the notch length. For Ti6Al4V, Liao and Duffy (1998) got to the same conclusion in their torsion experiments. It appears that AM50 is not different in that respect.

Figure 8 shows the normalized dynamic mechanical energy (divided by W_D of un-notched specimen, Table 3) as a function of the notch length for these alloys. From this figure, it appears again that no definite conclusion can be drawn as to the influence of the length of the defect on ASB formation, from an energy point of view. While this is expected for a low-hardening material such as Ti6Al4V, this observation is quite meaningful for the highly strain hardening AM50 alloy. In other words, the plastic flow properties of the material do not seem to govern the propensity to ASB failure in the presence of notches of various lengths.

To summarize, Figures 7 and 8 show that the influence of the notch length is not a governing parameter for ASB formation for the two investigated alloys. For notch lengths of up to 1 mm, these figures clearly show that, for a given notch root radius, both the failure strain and dynamic deformation energy do not vary significantly.

The influence of the notch root radius is examined next.

Notched SCS: influence of the root radius

The (normalized) failure strain is plotted as a function of the inverse root radius for the two alloys in Figure 9. The initial point is that of a smooth specimen (infinite root radius).

As the notches grow sharper, the dynamic failure strain decreases for both materials. It seems that Ti6Al4V possesses a higher notch sensitivity than AM50. Figure 10 shows the normalized (W_D , Table 3) dynamic deformation energy as a function of the notch root-radius. Figure 10 shows that the energy decreases as the notches grow sharper. For Ti6Al4V, this result is expected due to its small strain hardening capacity, as mentioned previously. However, AM50, which has a high strain

hardening capacity, exhibits a milder decrease in normalized dynamic energy. Figure 10 confirms the higher notch sensitivity of Ti6Al4V. The experimental results are too "noisy" to perform a statistically quantitative meaningful curve fit. However, visual examination of the data suggests a linear correlation between the dynamic deformation energy and the inverse notch root radius.

To summarize, Figures 9 and 10 show a clear influence of the notch root radius on both the failure strain and the dynamic deformation energy for ASB formation. This is particularly evident since all the investigated notch lengths are included in these figures. At this stage, additional information about the notch-tip fields must be gained by means of numerical simulations, as shown next.

Numerical model of the sheared notch

In the absence of an analytical solution for the fields ahead of the dynamically sheared notch, taking into account the variable radius of curvature, the problem was modeled numerically. Dynamic numerical analyses of 2 specimens with short notches were carried out using ANSYS (2005) finite element code. The model specimens contained 0.8 mm long notches, with root-radii of $\rho = 0.15$ and 0.30 mm respectively. A typical meshed specimen of $\rho=0.3$ mm notch radius is shown in Figure 11. The mesh comprises 32920 elements of type SOLID187, which are a higher order 3-D 10-node elements. SOLID187 has a quadratic displacement behavior, and it is well suited to model irregular meshes. For this mesh a satisfactory numerical convergence was obtained. Because of the symmetry of the problem, only one half of the specimen was modeled. The bottom face of the specimen was constrained vertically. In addition, one point of the bottom face was constrained in all directions. The upper face of the specimen was loaded with a vertical displacement of $d=-0.7$ mm in 35 μ s. The selected materials were the AM50 and Ti6Al4V alloys, whose mechanical characteristics were reported in Rittel et al. (2006) for AM50, and in the first section for Ti6AL4V. The solution scheme was implicit, together with a large strain formulation.

Results for AM50

According to Figure 9, the average failure strain for both $\rho = 0.3$ mm and $\rho = 0.15$ mm is $\hat{\epsilon}_{eqv} \cong 0.136$. The undeformed $\rho = 0.3$ mm and $\rho = 0.15$ mm notches are plotted in Figure 12, along with the dynamic deformation energy distribution at

failure ($\hat{\epsilon}_{eqv} \cong 0.136$) around it. This figure shows a higher deformation energy density on the upper half of the notch, which is (probably) the initial location for ASB formation. The average deformation energy at failure is $W_D^{AM50} = 3.1 \times 10^7 \text{ J/m}^3$ for the 2 notches. The maximum values observed in Figure 12 are $W_D^{0.3} \approx 3 \times 10^8 \text{ J/m}^3$ for $\rho = 0.3 \text{ mm}$, and $W_D^{0.15} \approx 5 \times 10^8 \text{ J/m}^3$ for $\rho = 0.15 \text{ mm}$. These values show that the smaller the notch, the higher the maximum deformation energy, and also that the local values near the notch tip are one order of magnitude higher than the average values along the gauge.

The dynamic deformation energy in the gauge section was calculated along a 45° inclined path shown in Figure 13. The evolution of the dynamic deformation energy for the 2 radii is plotted in Figure 14.

Figure 14 shows that the dynamic deformation energy at failure is uniform in the gauge section, except for the immediate vicinity of the notch (normalized distance = 1). The average calculated value at failure, irrespective of the notch root radius, is $W_D^{AM50} = 3.1 \times 10^7 \text{ J/m}^3$. Rittel et al. (2006) reported a typical experimental value of the dynamic deformation energy of $W_D^{AM50} = 4.04 \times 10^7 \text{ J/m}^3$ for un-notched AM50 specimens (Table 3). The normalized calculated average dynamic deformation energy at $\hat{\epsilon}_{eqv} \cong 0.136$ is therefore 0.76, which is slightly lower than the measured deformation energy (typically 0.85), as shown in Figure 10. Yet, the overall agreement between calculated and measure dynamic deformation energies is quite satisfactory. The presence of the notch does not affect the uniformity of the average dynamic deformation energy in the gauge section, nor does it affect the uniformity of the average effective stress and strain in the gauge section (Table 2). The calculations show that the effect of the notch is highly localized to roughly 3% of the gauge length, corresponding to $\sim 0.4 \text{ mm}$ from the notch tip. In this region, the maximum dynamic deformation energy density increases as the notch-radius decreases.

Results for Ti6Al4V

From Figure 9, the average failure strain of Ti6Al4V is $\hat{\epsilon}_{eqv} \cong 0.23$ and $\hat{\epsilon}_{eqv} \cong 0.21$, for $\rho = 0.3 \text{ mm}$ and $\rho = 0.15 \text{ mm}$, respectively. The dynamic deformation energy distribution around the undeformed notches at failure is plotted in Figure 15 for the 2

notch radii. Similar to the previous case, a higher concentration of energy is noticeable in the upper half of the notch.

The average deformation energy at $\hat{\epsilon}_{eqv} \cong 0.23$ ($\rho = 0.3$ mm) is $W_D^{0.3} = 3.3 \times 10^8$ J/m³. The maximum value observed in Figure 12 for $\rho = 0.3$ mm is $W_D^{0.3max} \approx 2 \times 10^9$ J/m³. The average deformation energy at $\hat{\epsilon}_{eqv} \cong 0.21$ ($\rho = 0.15$ mm) is $W_D^{0.15} = 2.9 \times 10^8$ J/m³. The maximum value for $\rho = 0.15$ mm is $W_D^{0.15max} \approx 2.3 \times 10^9$ J/m³. The normalized values of the dynamic deformation energy of notched specimens are therefore $W_D^{0.3num} = 0.95$ and $W_D^{0.15num} = 0.83$, which match quite well the measured values shown in Figure 10, namely $W_D^{0.3exp} = 0.82$ and $W_D^{0.15exp} = 0.75$. Like before, sharper notches experience higher levels of maximum dynamic deformation energy, whose values are about one order of magnitude higher than the average values obtained in the gauge section.

The distribution of the dynamic deformation energy along the gauge section is plotted in Figure 15 for both $\rho = 0.3$ mm and $\rho = 0.15$ mm. It can be noted that the deformation energy starts to increase noticeably from a distance of about 25% of the path length, whereas, for AM50, only 3% of the path length was affected. Therefore the presence of a notch has a much larger influence on the averaged measured values for Ti6Al4V.

The main results of the numerical study are summarized in Table 4.

DISCUSSION

The present work comprises three parts. The first part addresses dynamic deformation energy as a macroscopic criterion for ASB formation. Similar results were previously shown for AM50 alloy (Rittel et al., 2006) and here, it is again shown that, whereas a critical strain criterion does not accurately reflect the overall thermomechanical history of Ti6Al4V, the dynamic deformation energy remains rather constant irrespective of large quasi-static prestrain levels. In addition, this quantity is not influenced by the specimen initial temperature, even if the latter exceeds by far that which results from homogeneous adiabatic heating. These results will not be further discussed here, as they are identical to those obtained previously for another material, and are mostly shown here to show that the dynamic mechanical energy concept

applies to Ti6Al4V too. This concept is used throughout this work to study the influence of geometrical imperfections on ASB formation.

The influence of geometrical imperfections is the main theme of this work. As stated in the introduction, little experimental data is available on this issue, except for the work of Duffy and coworkers (Marchand and Duffy (1988), Duffy and Chi (1992), Liao and Duffy (1998)), which is closely related to that of Molinari and Clifton (1987). It should be emphasized that Duffy's experiments consist of torsion of thin walled specimens containing a small thickness variation. By analogy with fracture mechanics, these are anti-plane shear experiments (mode III), whereas our experiments are of the mode II type. Consequently, one could not establish a direct comparison between the 2 kinds of experiments, even if they both are shear experiments. The analogy between fracture mechanics and adiabatic shear banding can be found in Grady's work (1992), in which the notion of shear band toughness is introduced. This toughness is a measure of energy for the propagating ASB, as is the dynamic deformation energy for its initiation. Keeping the above-mentioned distinction between the 2 types of experiments in mind, the present results are nevertheless the first systematic investigation of the influence of the length and the root-radius of the defect, when these are considered separately.

The present study shows that, both in terms of strain and deformation energy, the length of the geometrical imperfection does not significantly influence adiabatic shear failure of the investigated materials. One should of course restrict this statement to the relatively short notches considered in this work, and the only apparent result is that the very introduction of a defect seems to slightly affect ASB formation. But again, once a defect is introduced, its length does not affect the results in itself. And indeed, when a correlation is sought between either the failure strain or the dynamic deformation energy with the notch length, it is evident that if one specific root radius is selected, the above mentioned parameters do not significantly vary with the notch length (Figures 7 and 8). By contrast, the present experiments clearly show that the root-radius of the notch is a key parameter that influences the propensity for ASB formation, whether in terms of failure strain or dynamic deformation energy (Figures. 9 and 10). This result supports qualitatively the analytical work of Dinzart et al. (1994) who selected the critical strain as a failure criterion. The two investigated alloys respond differently to the sharpness of the notch. The data obtained for AM50 is noisier than that gathered for Ti6Al4V, but altogether, AM50 is globally less notch-

sensitive than Ti6Al4V. A clear trend can nevertheless be identified, namely that both the failure strain and the dynamic deformation energy decrease for sharper notches, in different proportions for each material.

The third part of this work is a thorough numerical simulation aimed at capturing the salient features of the notch-tip fields in both materials, for 2 different notch root-radii. The first common feature is the expected concentration of energy in the immediate vicinity of the notch tip (more precisely in its upper half). Here, the local dynamic deformation energy levels can be higher than the average level in the gauge section by one order of magnitude. This high density of energy is most likely responsible for the local initiation of ASB's, keeping in mind that the local density of energy is material dependent (strain concentration). The numerical study also shows that the calculated average dynamic deformation energy is rather similar to that measured experimentally, as shown in Table 4. The high local energy values are most likely responsible for the onset of ASB formation, and might be the basis for a local failure criterion, not addressed in the present work. Yet, the measured average (global) energy values can be used as a global criterion for ASB failure.

A final important remark must be made concerning thermal softening effects and shear localization. While ASB nucleation without deliberate geometrical imperfection was shown to be independent of the global temperature in the two investigated materials, the present results on localized nucleation show a large local concentration of deformation energy. This, in turn, is expected to induce significant local thermal softening, thus precipitating the dynamic failure process.

CONCLUSIONS

This work is a joint experimental-numerical study of the effects of geometrical imperfections on adiabatic shear failure.. Two materials were investigated: AM50 and Ti6Al4V alloys. For the latter, preliminary experiments on un-notched specimens show the relevance of the dynamic deformation energy, just as reported for AM50 (Rittel et al., 2006). Two geometrical parameters of the notch were systematically considered in a series of experiments. These are the notch *length* and notch *root-radius*, which had not been addressed *separately* in previous work.

The main conclusions of this work are:

1. Adiabatic shear failure from a geometrical imperfection is influenced by the sharpness more than by the size of the imperfection, in agreement with Dinzart et al.'s (1994) analytical results.
2. Numerical simulations of notched specimens show a distinct concentration of energy in the vicinity of the notch.
3. This concentration is likely to induce pronounced local thermal effects that should promote localized ASB nucleation, as opposed to the homogeneous nucleation process for which thermal softening may not always be the main or only factor.
4. For the high strain hardening AM50 alloy, the high concentration of energy spans over less than 3% of the gauge length, whereas for the low strain hardening Ti6Al4V, about 25% of the gauge length is affected by the notch. The average dynamic deformation energy in the gauge section is affected accordingly.
5. A very good agreement is observed between the calculated and the measured average values of the average dynamic deformation energy in the gauge section, for various notch root radii in the two materials.
6. The measured dynamic deformation energy can therefore be considered as a valid *global* quantitative measure of the propensity for ASB formation.

Acknowledgement: The support of the Israel Science Foundation (grant # 2002968) is gratefully acknowledged. DR would like to thank A. Molinari for many fruitful discussions.

References

- ANSYS, Release 8.0, 2005, Ansys Inc.
- Bai Y.L., Dodd B., 1992. *Adiabatic Shear Localization-Occurrence, Theories and Applications*. Pergamon Press. Oxford, UK.
- Batra, R.C., Kim, C.H., 1990a. Adiabatic shear banding in elastic-viscoplastic nonpolar and dipolar materials. *Int. J. Plasticity* 6, 127-141.
- Batra, R.C., Kim, C.H., 1990b. The interaction among adiabatic shear bands in simple and dipolar materials. *Int. J. Eng. Sci.* 28, 927-942.
- Batra R. C., Gummalla R. R., 2000. Effect of material and geometric parameters on deformations near the notch-tip of a dynamically loaded prenotched plate. *Int. J. Fracture*. 101, 99-140.
- Bever M. B., Holt D. L. and Titchener A. L., 1973. *Prog. Mater. Sci.* 17, 5.
- Clos R., Schreppel U. and Veit P. 2003. Microstructure and temperature during shear band formation in different metallic materials, *J. de Phys. IV* 110(1), 111-115.
- Dinzart F., Fressengeas C. and Molinari A., 1994. The catastrophic development of shear localization in thermoviscoplastic materials, *J. de Phys. IV (C8)*, 435-440.
- Dorogoy A., Rittel D., 2005a. Numerical validation of the shear compression specimen (SCS). Part I: Quasi-static large strain testing, *Exp. Mech.* 45, 167-177.
- Dorogoy A., Rittel D., 2005b. Numerical validation of the shear compression specimen (SCS). Part II: Dynamic large strain testing, *Exp. Mech.* 45, 178-185.
- Duffy J., Chi Y. C., 1992. On the measurement of local strain and temperature during the formation of adiabatic shear bands. *Mater. Sci. Eng. A157*, 195-210.
- Grady DE., 1992. Properties of an adiabatic shear-band process zone, *J. Mech. Phys. Solids* 40(6), 1197-1215.
- Kolsky H., 1949. *Stress Waves in Solids*. Dover Publications, New York USA.
- Liao S. C., Duffy J., 1998. Adiabatic shear bands in a Ti6Al4V titanium alloy. *J. Mech. Phys. Solids*. 46(11), 2201-2231.
- Marchand A. and Duffy J. 1988. An Experimental Study of the Formation process of Adiabatic shear bands in a structural steel, *J. Mech. Phys. Solids*, 36(3) 251-283.
- Merzer A. M., 1982. Modeling of adiabatic shear band development from small imperfections, *J. Mech. Phys. Solids* 30, 323-338.
- Meyers M. A., 1994. *Dynamic behavior of materials*. J. Wiley & Sons, New York, USA.
- Molinari A., Clifton R. J., 1987. Analytical characterization of shear localization in thermoviscoplastic materials, *Trans. ASME* 54, 806-812.
- Nowacki W.K., Zarka J., 1979. Sur le champ des températures obtenues en thermoélastoviscoplasticité, *Arch. of Mech.* 26 No. 4, 701-715.
- Rittel, D., Lee, S. and Ravichandran, G., 2002. A shear compression specimen for large strain testing, *Exp. Mech.* 42 No. 1, 58-64.
- Rittel D., Wang Z. G., Merzer M., 2006. Adiabatic shear failure and dynamic stored energy of cold work. *Phys. Rev. Letters*. 96, 075502.
- Tresca, H., 1879. Sur la fluidité et l'écoulement des corps solides. *Annales du Conservatoire des Arts et Métiers*, 41 tome XI 1^{er} fasc., 153-160.
- Wright, T.W., 2002. *The Physics and Mathematics of Adiabatic Shear Bands*. Cambridge University Press, Cambridge.

Zener C. , Hollomon J. H., 1944. Effect of strain rate upon plastic flow of steel. J. of App. Phys., 15(1), 22-32.

FIGURE CAPTIONS

- Figure 1.** Schematic representation of the Shear Compression Specimen (SCS). All dimensions are in millimeters. D , $h = \sqrt{2} w$, and t are the geometrical parameters used for equivalent stress and equivalent strain determination. For the AM50 specimens, $D=10\text{mm}$, $w = 1.5\text{mm}$ $t=2.5\text{mm}$. For the Ti6Al4V specimens, $D=10\text{ mm}$, $w = 2\text{ mm}$ $t=2.5\text{mm}$.
- Figure 2:** Typical small notch geometry
- Figure 3:** Composite stress-strain curves for static-dynamic tests. Note that the total strain to failure (indicated by arrows) increases with the level of quasi-static pre-strain.
- Figure 4:** Plot of the dynamic deformation energy of Ti6Al4V as a function of the normalized pre-strain ($\frac{\epsilon_{\text{pre-strain}}}{\epsilon_{\text{FS}}^{\text{Ti6Al4V}}} \times 100$) at $\dot{\epsilon} \approx 3000\text{s}^{-1}$. Note that the energy is quite constant up to normalized pre-strain levels of the order of 0.45, beyond which it decreases.
- Figure 5:** Stress-strain curves for dynamic-dynamic test of Ti6Al4V ($\dot{\epsilon} \approx 3000\text{s}^{-1}$). Failure is indicated by arrows. The solid line indicates a monotonic test.
- Figure 6A:** Dynamic stress strain curves of Ti4Al4V at different temperatures
- Figure 6B:** Dynamic deformation energy of Ti4Al4V at different initial test temperatures. The dashed line indicates the maximum homogeneous temperature in the gauge section. Note that the dynamic energy remains relatively constant in this range of temperatures (normalized by $T_m=1873\text{K}$).
- Figure 7A:** Normalized ($\epsilon_{\text{FD}}^{\text{AM50}}=0.16$) failure strain vs. notch length (AM 50). Results for all the radii are plotted together. Zero length corresponds to macroscopically smooth specimens. Specimens that did not crack from the notch are also included. The failure strain is independent of the notch length.
- Figure 7B:** Normalized failure strain ($\epsilon_{\text{FD}}^{\text{Ti6Al4V}}=0.25$) vs. notch length (Ti6Al4V). Results for all the radii are plotted together. Zero length corresponds to macroscopically smooth specimens. Specimens that did not crack from the notch are also included. The failure strain is independent of the notch length.
- Figure 8A:** Normalized (w/r un-notched specimen, $W_D^{\text{AM50}}=4.04 \times 10^7\text{J/m}^3$) dynamic deformation energy vs. notch length (AM 50). Results for all the radii are plotted together. Zero length corresponds to macroscopically smooth specimens. Specimens that did not crack from the notch are also included. The dynamic deformation energy is independent of the notch length.

- Figure 8B:** Normalized (w/r un-notched specimen $W_D^{\text{Ti6Al4V}} = 3.48 \times 10^8 \text{ J/m}^3$) dynamic deformation energy vs. notch length (Ti6Al4V). Results for all the radii are plotted together. Zero length corresponds to macroscopically smooth specimens. Specimens that did not crack from the notch are also included. The dynamic deformation energy is independent of the notch length.
- Figure 9:** Normalized (w/r un-notched specimen, Table 3) dynamic failure strain vs. inverse notch root-radius of AM50 (A) and Ti6Al4V (B). All the notch lengths are included.
- Figure 10:** Normalized (w/r un-notched specimen, Table 3) dynamic deformation energy vs. inverse notch root-radius of AM50 (A) and Ti6Al4V (B). All the notch lengths are included.
- Figure 11:** A meshed notched SCS: A: Whole mesh, B: Detailed view of the notch-tip.
- Figure 12 :** The distribution of the dynamic deformation energy density around the undeformed 0.8 mm long notch in AM50. A: $\rho = 0.3 \text{ mm}$. B: $\rho = 0.15 \text{ mm}$.
- Figure 13:** Path used for energy calculations along the gauge
- Figure 14:** AM50: A comparison of the dynamic deformation energy at failure ($\hat{\epsilon}_{\text{eqv}} \cong 0.136$) along the gauge section for $\rho = 0.15 \text{ mm}$ and $\rho = 0.30 \text{ mm}$. Note the similarity of the energy distribution, irrespective of the notch-tip radius.
- Figure 15:** The distribution of the dynamic deformation energy density around the undeformed 0.8 mm long notch in Ti6Al4V. A: $\rho = 0.3 \text{ mm}$. B: $\rho = 0.15 \text{ mm}$. Note the wide area of influence of the notch with respect to AM50 (Figure 12).
- Figure 16:** A comparison of the dynamic deformation energy at failure ($\hat{\epsilon}_{\text{eqv}} \cong 0.23$ and $\hat{\epsilon}_{\text{eqv}} \cong 0.21$) along the gauge section, for $\rho = 0.30 \text{ mm}$ and $\rho = 0.15 \text{ mm}$.

FIGURES

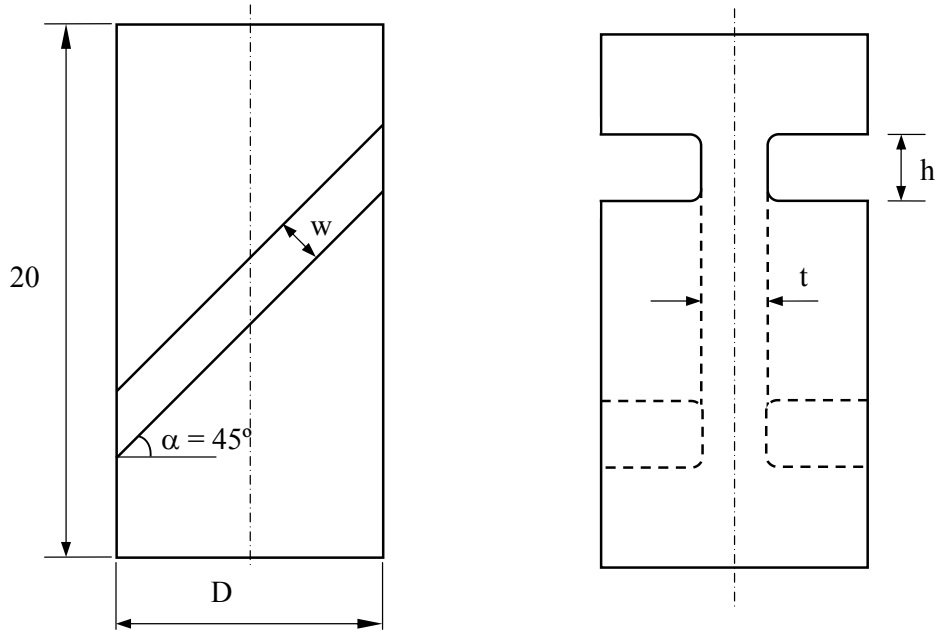


Figure 1. Schematic representation of the Shear Compression Specimen (SCS). All dimensions are in millimeters. D , $h = \sqrt{2} w$, and t are the geometrical parameters used for equivalent stress and equivalent strain determination. For the AM50 specimens, $D=10\text{mm}$, $w = 1.5\text{mm}$ $t=2.5\text{mm}$. For the Ti6AL4V specimens, $D=10\text{ mm}$, $w = 2\text{ mm}$ $t=2.5\text{mm}$.

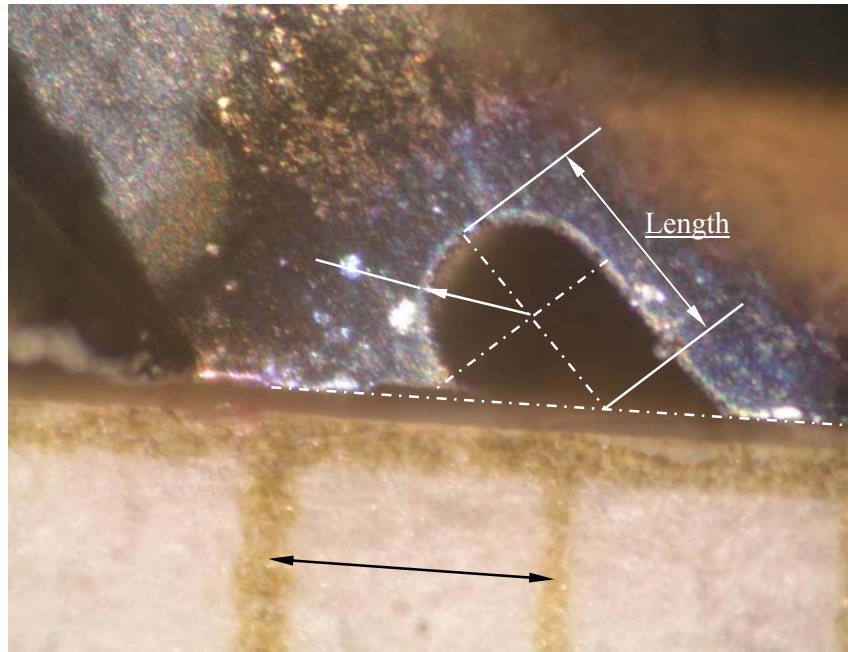


Figure 2: Typical small notch geometry

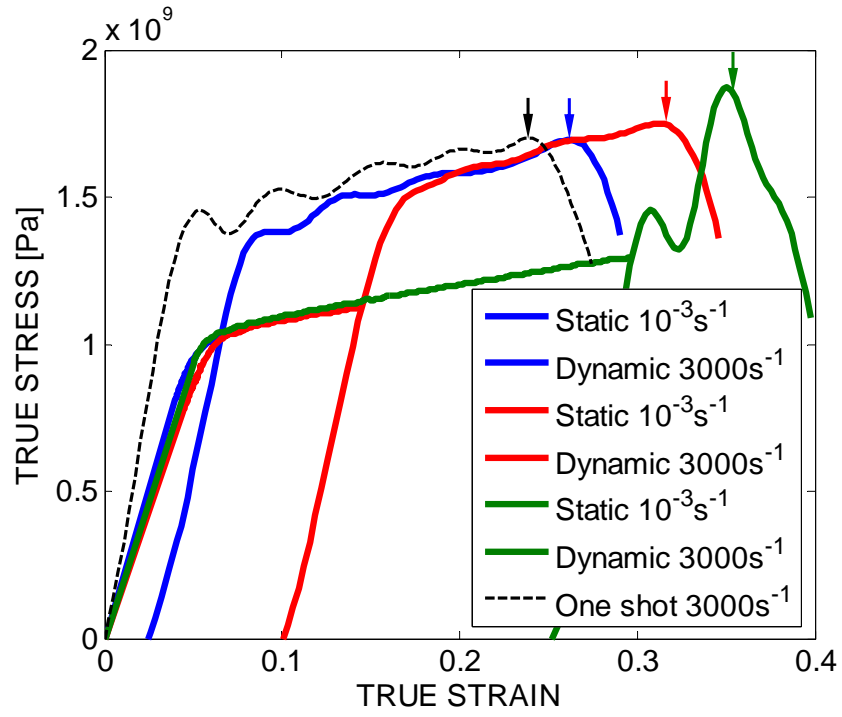


Figure 3: Composite stress-strain curves for static-dynamic tests. Note that the total strain to failure (indicated by arrows) increases with the level of quasi-static pre-strain.

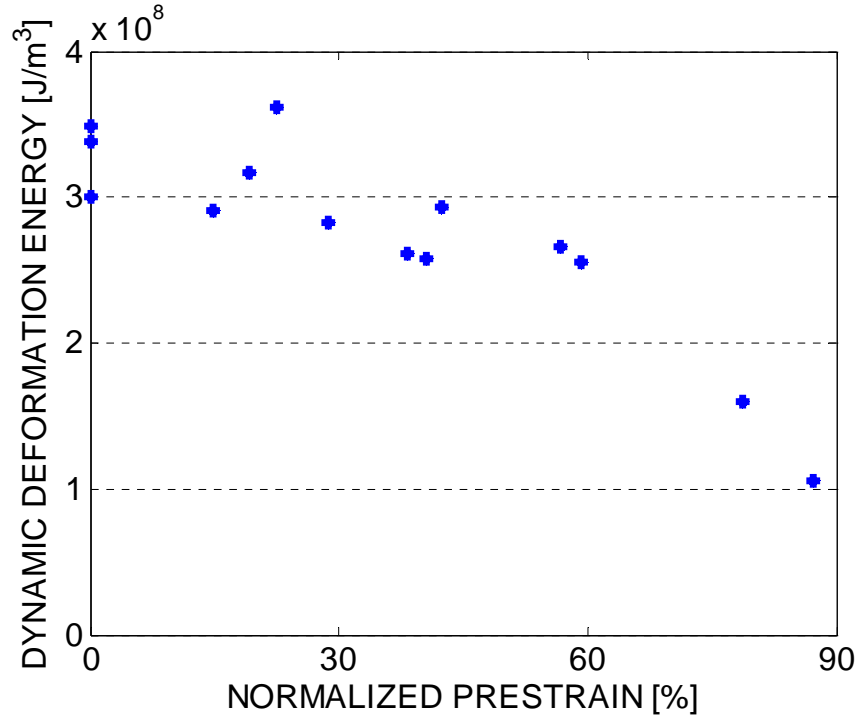


Figure 4: Plot of the dynamic deformation energy of Ti6Al4V as a function of the normalized pre-strain ($\frac{\epsilon_{\text{pre-strain}}}{\epsilon_{\text{FS}}} \times 100$) at $\dot{\epsilon} \approx 3000 \text{s}^{-1}$. Note that the energy is quite constant up to normalized pre-strain levels of the order of 0.45, beyond which it decreases.

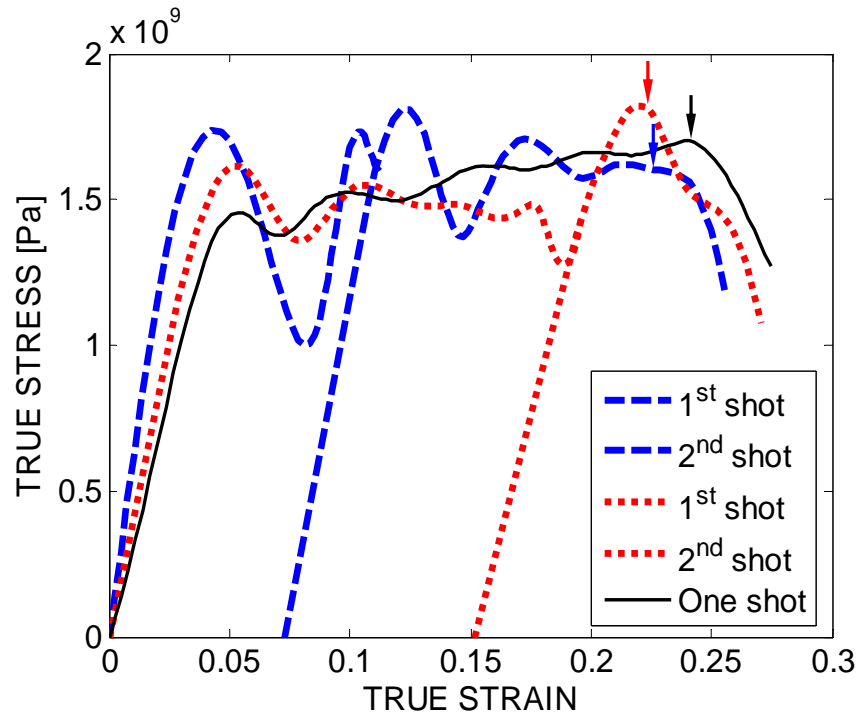


Figure 5: Stress-strain curves for dynamic-dynamic test of Ti6Al4V ($\dot{\epsilon} \approx 3000 \text{ s}^{-1}$). Failure is indicated by arrows. The solid line indicates a monotonic test.

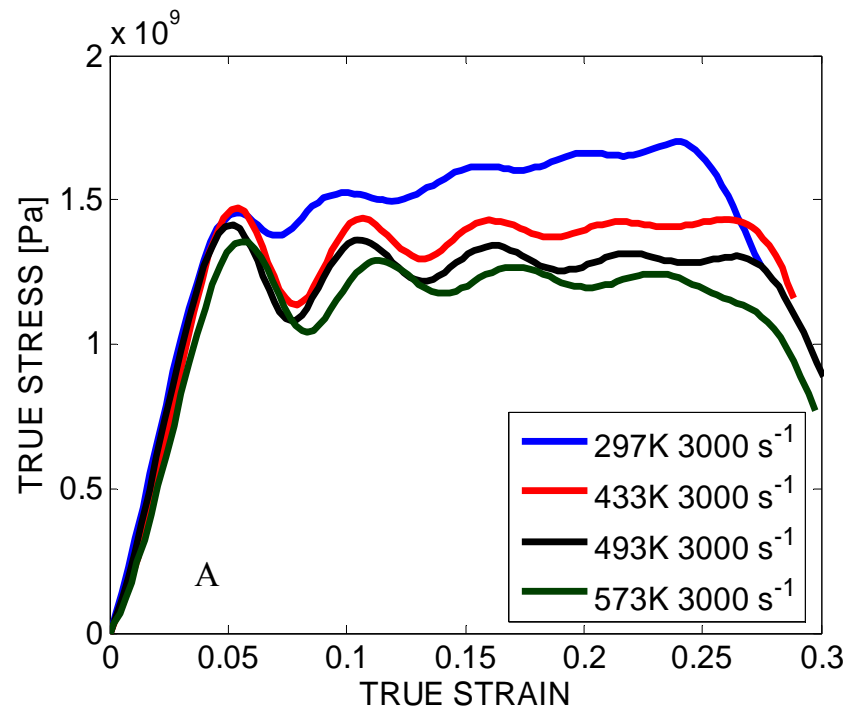


Figure 6A: Dynamic stress strain curves of Ti4Al4V at different temperatures

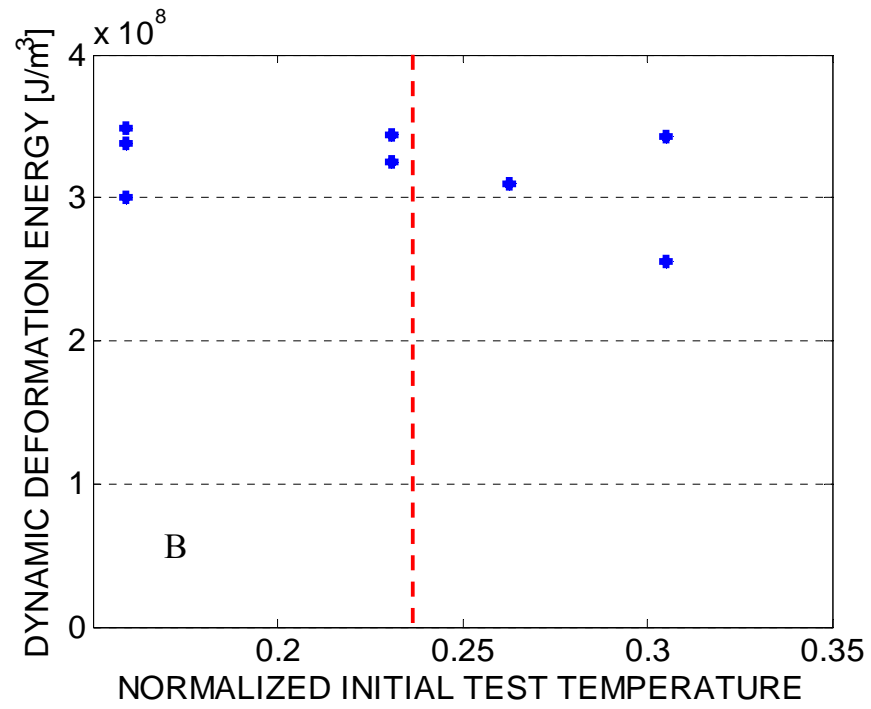


Figure 6B: Dynamic deformation energy of Ti4Al4V at different initial test temperatures. The dashed line indicates the maximum homogeneous temperature in the gauge section. Note that the dynamic energy remains relatively constant in this range of temperatures (normalized by $T_m=1873\text{K}$).

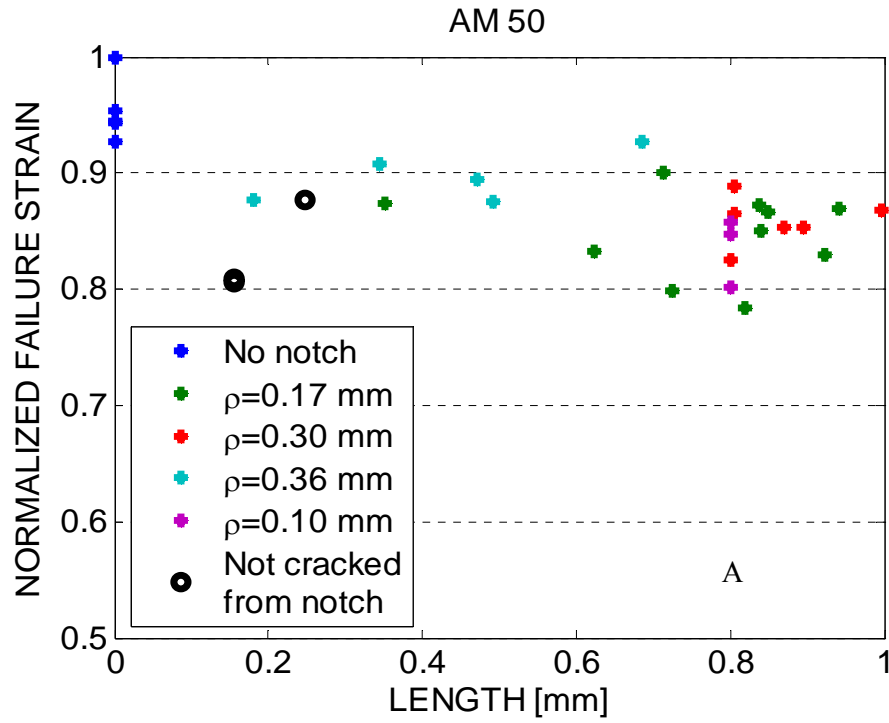


Figure 7A: Normalized ($\epsilon_{FD}^{AM50}=0.16$) failure strain vs. notch length (AM 50). Results for all the radii are plotted together. Zero length corresponds to macroscopically smooth specimens. Specimens that did not crack from the notch are also included. The failure strain is independent of the notch length.

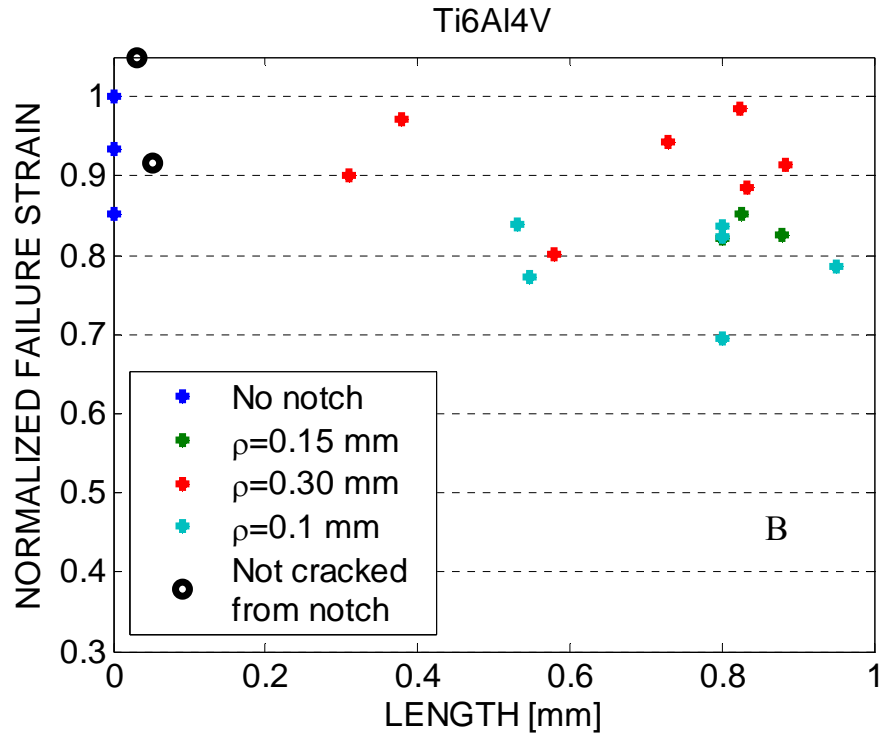


Figure 7B: Normalized failure strain ($\varepsilon_{FD}^{Ti6Al4V}=0.25$) vs. notch length (Ti6Al4V). Results for all the radii are plotted together. Zero length corresponds to macroscopically smooth specimens. Specimens that did not crack from the notch are also included. The failure strain is independent of the notch length.

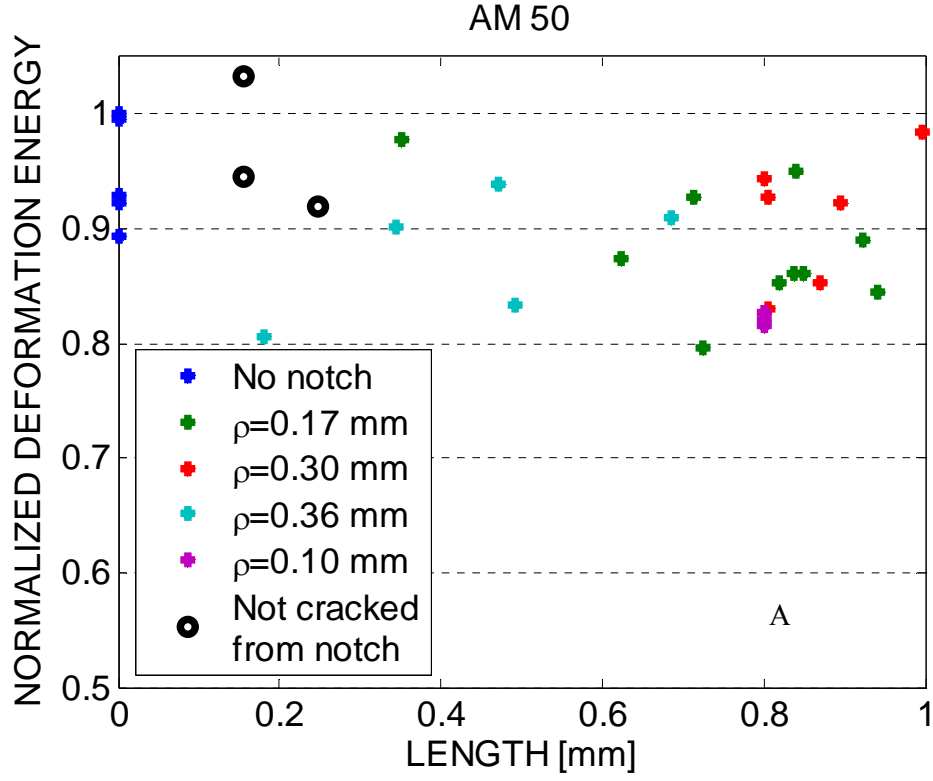


Figure 8A: Normalized (w/r un-notched specimen, $W_D^{AM50} = 4.04 \times 10^7 \text{ J/m}^3$) dynamic deformation energy vs. notch length (AM 50). Results for all the radii are plotted together. Zero length corresponds to macroscopically smooth specimens. Specimens that did not crack from the notch are also included. The dynamic deformation energy is independent of the notch length.

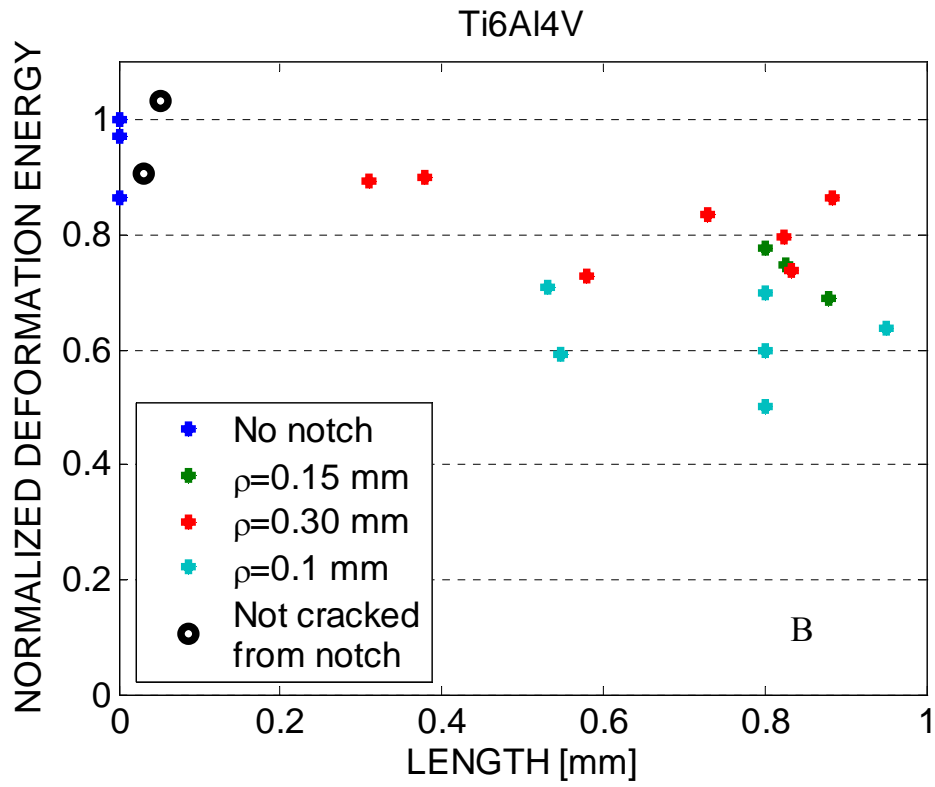


Figure 8B: Normalized (w/r un-notched specimen $W_D^{\text{Ti6Al4V}} = 3.48 \times 10^8 \text{ J/m}^3$) dynamic deformation energy vs. notch length (Ti6Al4V). Results for all the radii are plotted together. Zero length corresponds to macroscopically smooth specimens. Specimens that did not crack from the notch are also included. The dynamic deformation energy is independent of the notch length.

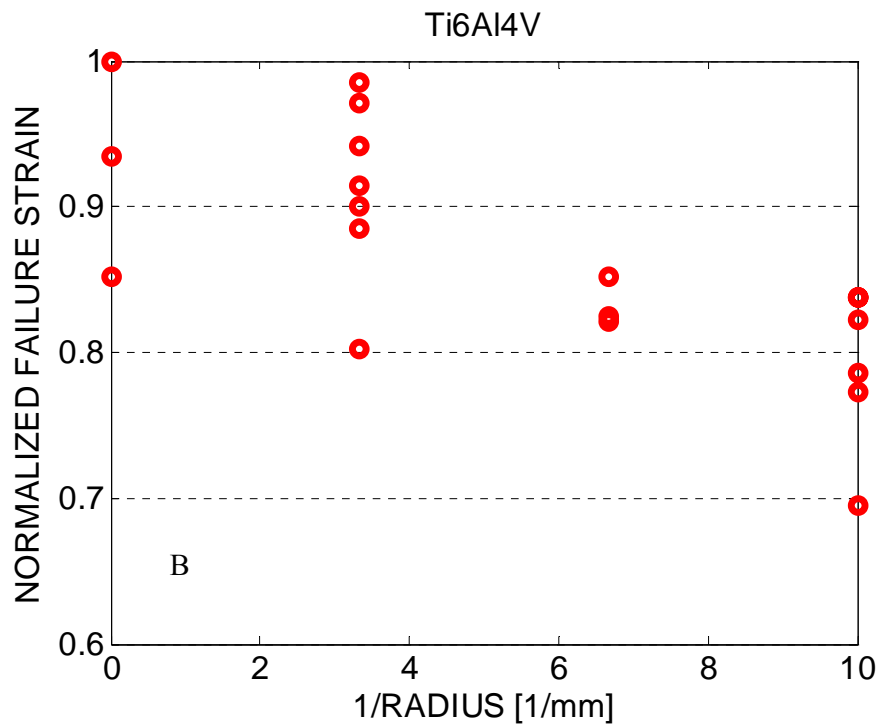
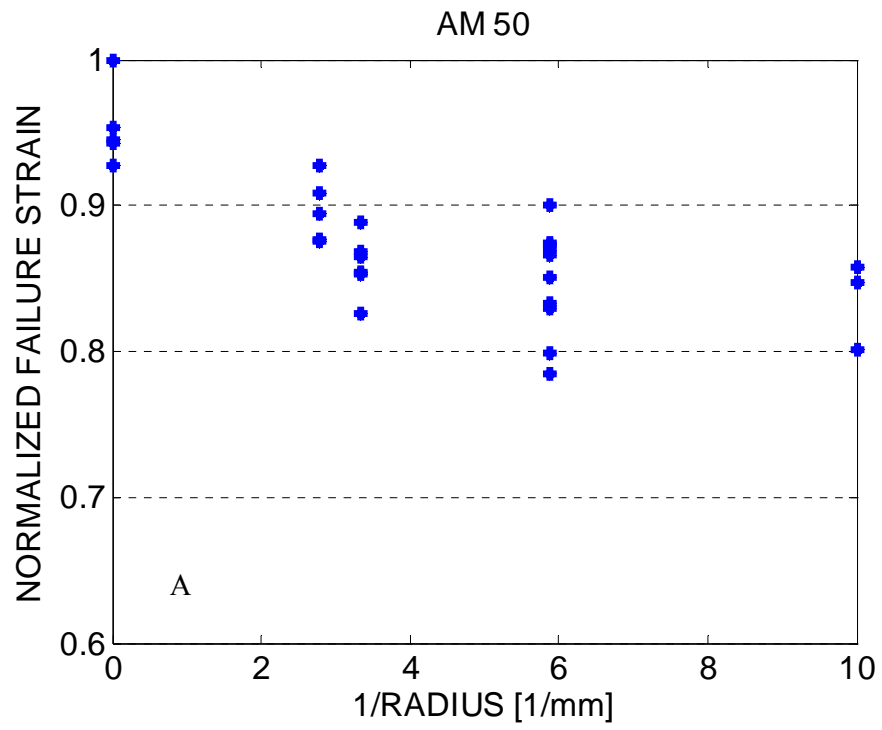


Figure 9: Normalized (w/r un-notched specimen, Table 3) dynamic failure strain vs. inverse notch root-radius of AM50 (A) and Ti6Al4V (B). All the notch lengths are included.

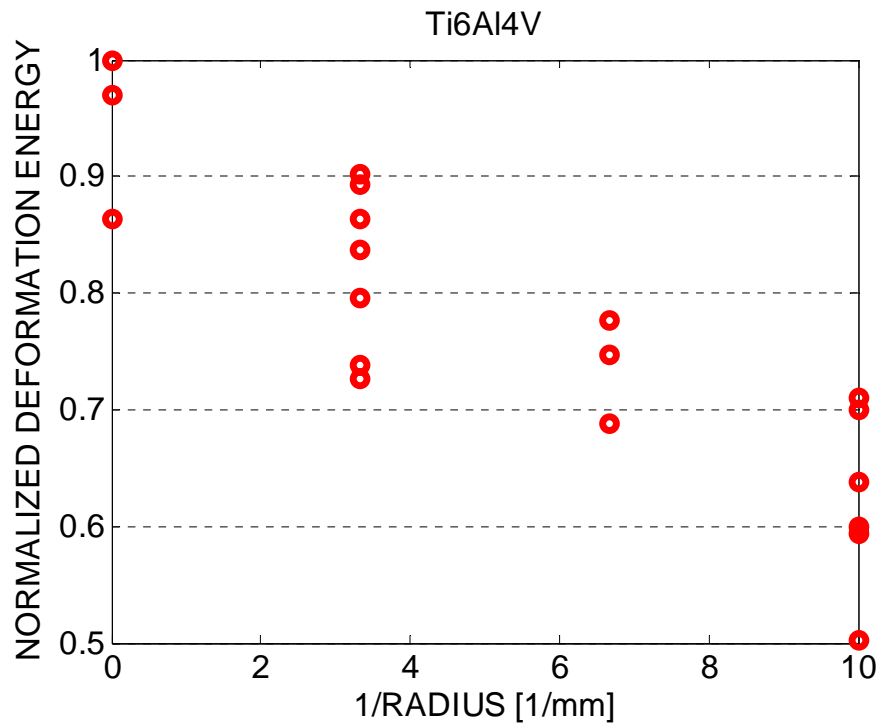
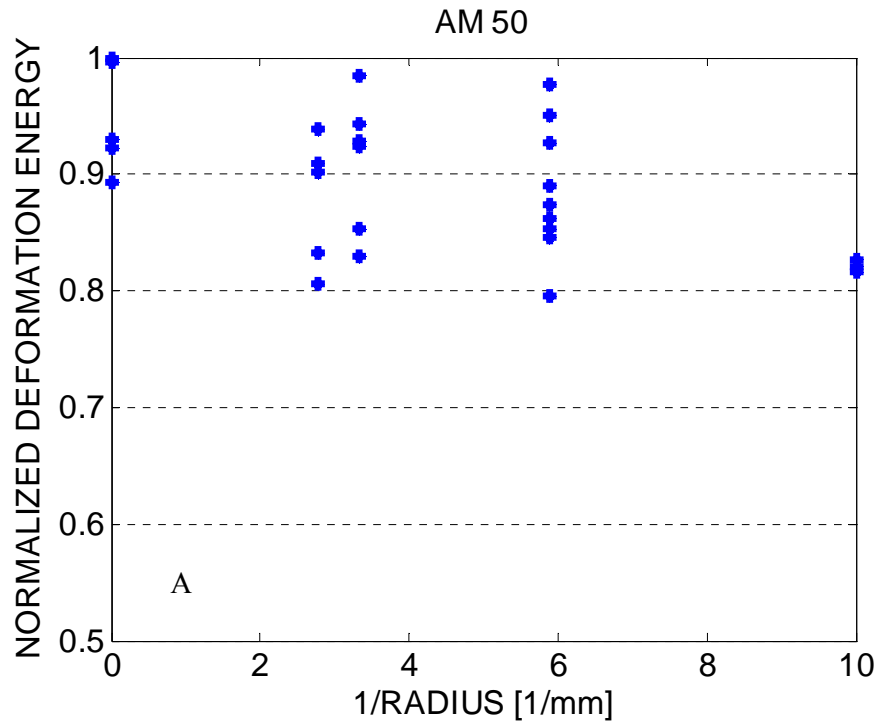
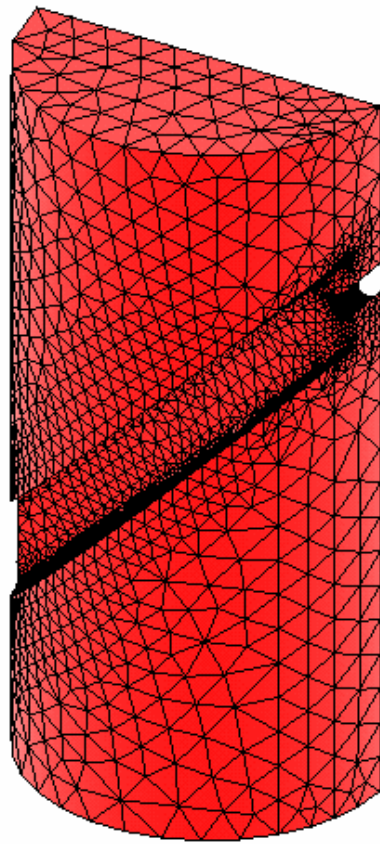
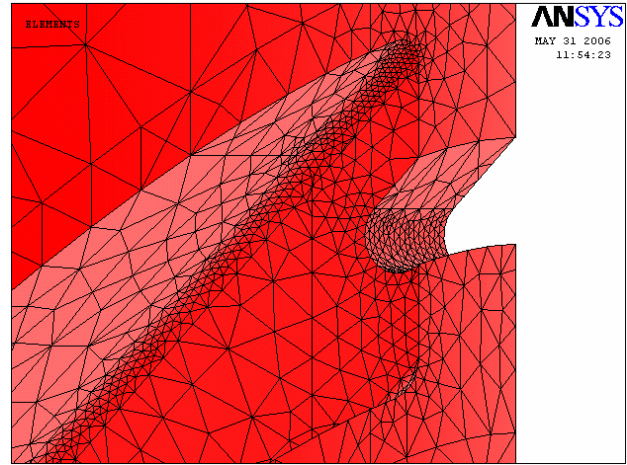


Figure 10: Normalized (w/r un-notched specimen, Table 3) dynamic deformation energy vs. inverse notch root-radius of AM50 (A) and Ti6Al4V (B). All the notch lengths are included.

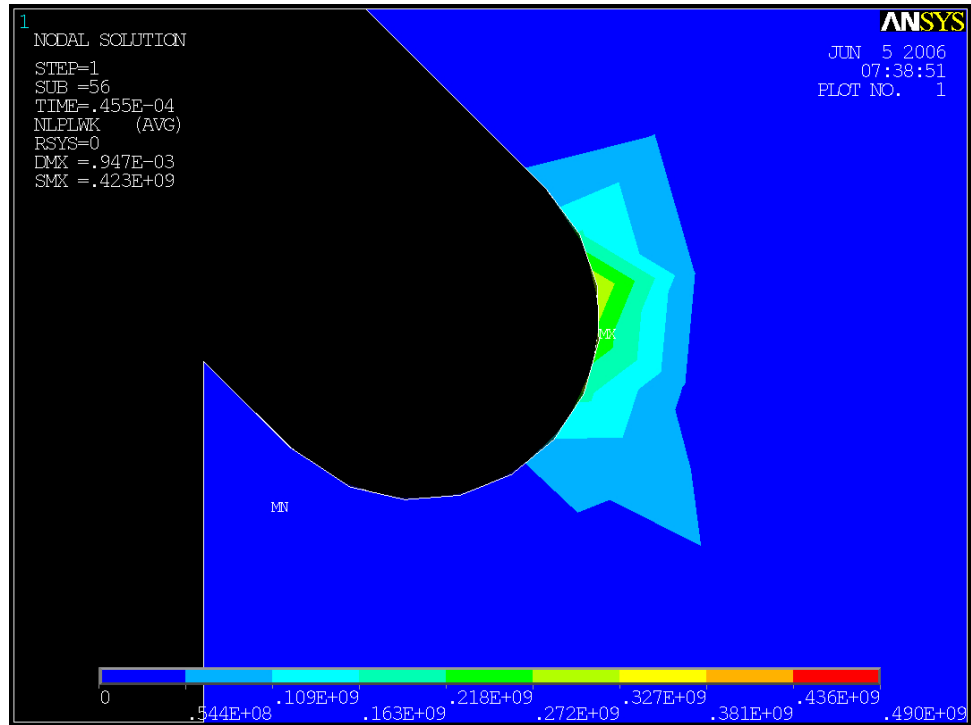


A

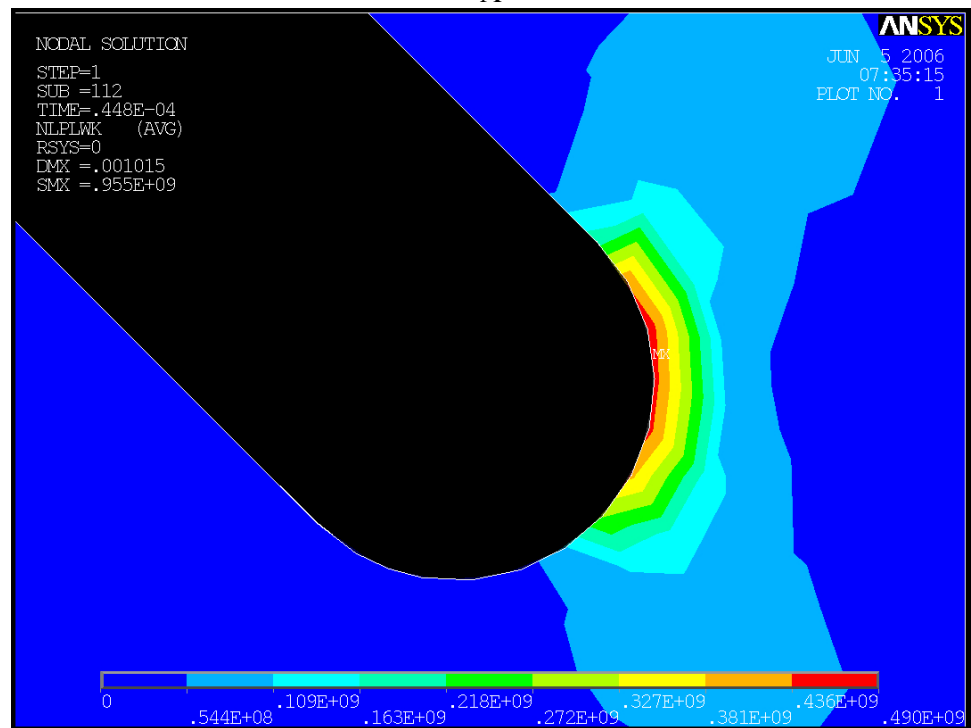


B

Figure 11: A meshed notched SCS: A: Whole mesh, B: Detailed view of the notch-tip.



A



B

Figure 12 : The distribution of the dynamic deformation energy density around the undeformed 0.8 mm long notch in AM50. A: $\rho = 0.3$ mm. B: $\rho = 0.15$ mm.

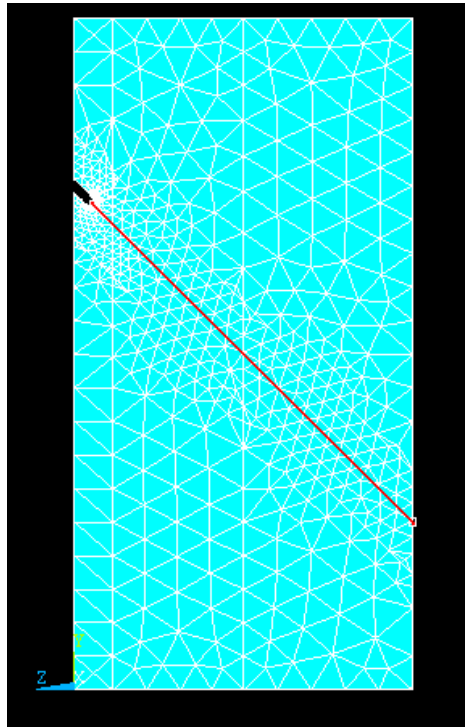


Figure 13: Path used for energy calculations along the gauge

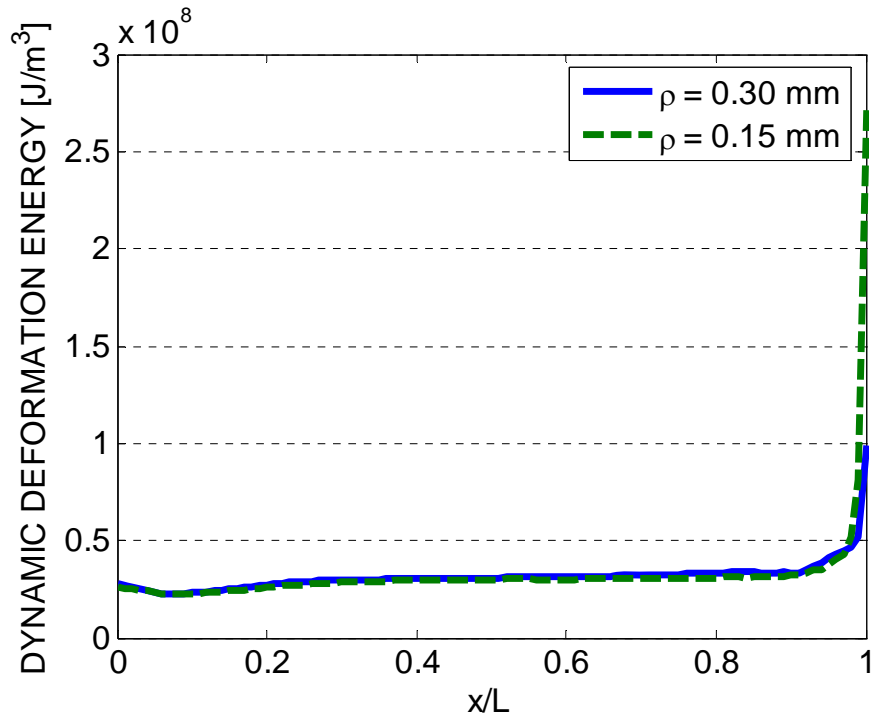


Figure 14: AM50: A comparison of the dynamic deformation energy at failure ($\hat{\epsilon}_{\text{eqv}} \cong 0.136$) along the gauge section for $\rho = 0.15$ mm and $\rho = 0.30$ mm. Note the similarity of the energy distribution, irrespective of the notch-tip radius.

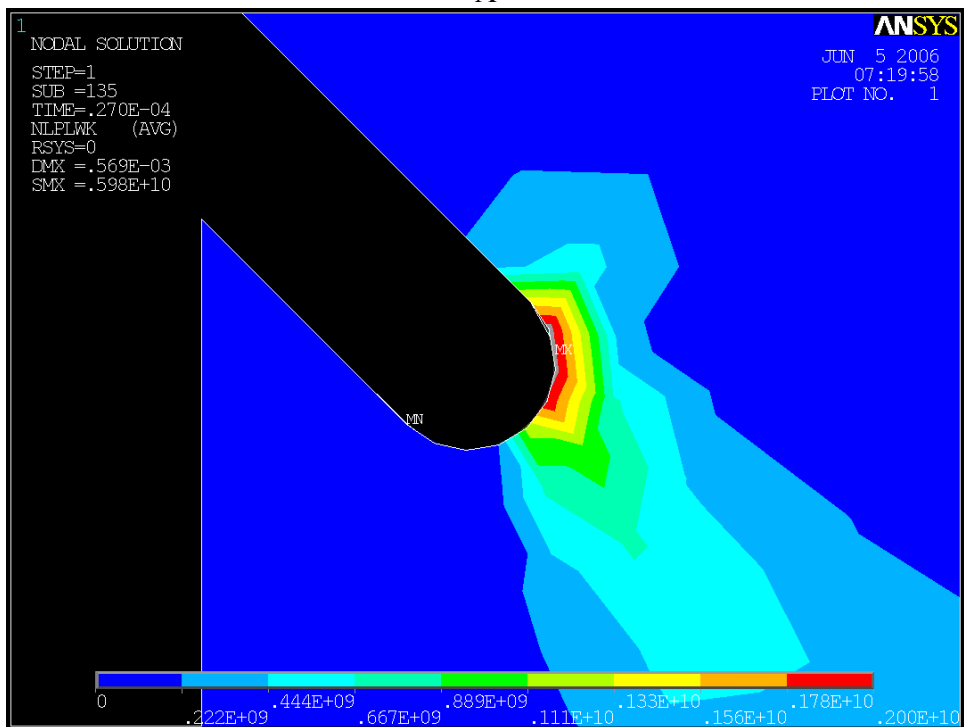
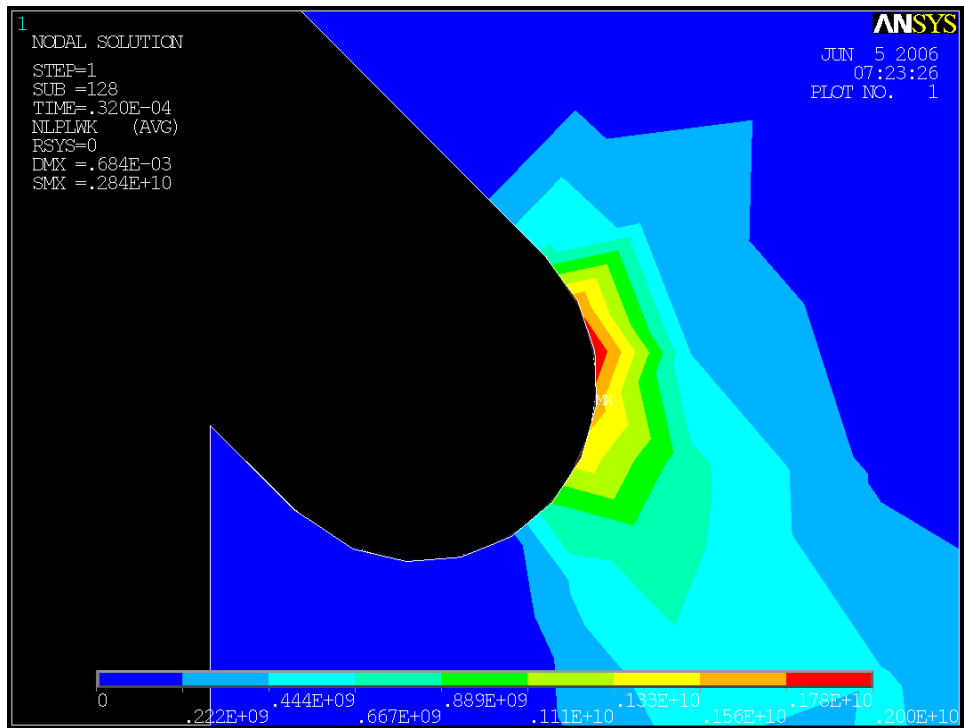


Figure 15 : The distribution of the dynamic deformation energy density around the undeformed 0.8 mm long notch in Ti6Al4V. A: $\rho = 0.3$ mm. B: $\rho = 0.15$ mm. Note the wide area of influence of the notch with respect to AM50 (Figure 12).

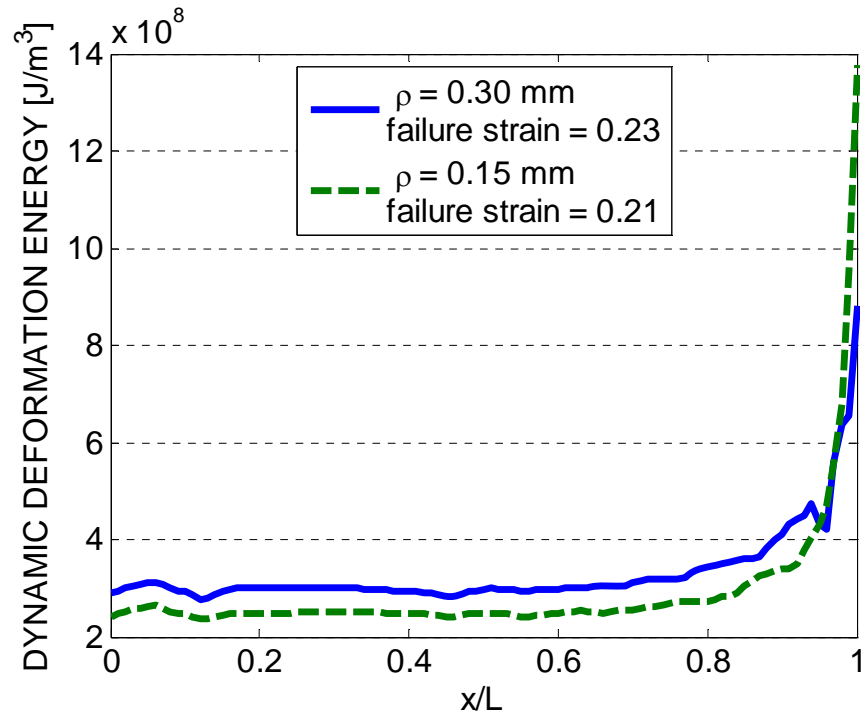


Figure 16: A comparison of the dynamic deformation energy at failure ($\hat{\epsilon}_{\text{eqv}} \cong 0.23$ and $\hat{\epsilon}_{\text{eqv}} \cong 0.21$) along the gauge section, for $\rho = 0.30$ mm and $\rho = 0.15$ mm.

TABLES

Notch Radius [mm]	Length [mm]	# specimens per alloy
0.15	0.2	3
0.15	0.4	3
0.15	0.6	3
0.15	0.8	3
0.30	0.2	3
0.30	0.4	3
0.30	0.6	3
0.30	0.8	3

Table 1: Geometrical notch parameters and number of specimens for each tested alloy

Material	ρ notch [mm]	K_1	K_2	K_3	K_4	K_5	d_y [mm]	ε_y
Mg AM50	All specimens	1.02	0.70	0.675	-1.4	1.25	0.06	0.01
Ti6Al4V	Smooth	0.96	0.18	1.133	0	0	0.141	0.0136
Ti6Al4V	0.30	1.05	0.18	1.230	0	0	0.126	0.0136
Ti6Al4V	0.15	1.00	0.18	1.314	0	0	0.128	0.0136
Ti6Al4V	0.10	0.98	0.18	1.343	0	0	0.128	0.0136

Table 2: K coefficients for the two investigated alloys. Ti6Al4V has different sets of K coefficients for each investigated notch root radius. Smooth specimens are described by an infinite notch root radius.

Material	Static failure strain	Dynamic failure strain	Dynamic deformation energy [J/m ³]
Ti6Al4V	$\epsilon_{FS}^{Ti6Al4V} = 0.34$	$\epsilon_{FD}^{Ti6Al4V} = 0.25$	$W_D^{Ti6Al4V} = 3.48 \times 10^8$
AM50	$\epsilon_{FS}^{AM50} = 0.14$	$\epsilon_{FD}^{AM50} = 0.16$	$W_D^{AM50} = 4.04 \times 10^7$

Table 3: Summary of the mechanical properties of the two investigated alloys.

Material	Experimental normalized W	Calculated normalized W	$\Delta_{\text{exper-numer}}$ [%]
AM50 – $\rho=0.15$ mm	0.85	0.76	-10.5
AM50 – $\rho=0.30$ mm	0.85	0.76	-10.5
Ti6Al4V – $\rho=0.15$ mm	0.75	0.83	+11
Ti6Al4V – $\rho=0.30$ mm	0.82	0.95	+15

Table 4: Experimental and calculated normalized dynamic deformation energies (W) for the two investigated alloys and root radii. The right most column indicates the difference between the experimental and calculated values.